Linear stability analysis of thermoviscous instability in immiscible displacement

Christopher Nilsen*
Department of Physics and Technology, University of Bergen, Allégaten 55, N-5007 Bergen, Norway

(Received 13 January 2018; published 29 June 2018)

We study the thermoviscous fingering instability problem that develops when an injected fluid is displacing a fluid with different temperature and viscosity in a Hele-Shaw cell or porous medium. Using linear stability theory, we show how the thermal front caused by the different temperature of the injected fluid impacts the growth rate of instabilities on an immiscible radial displacement front. The immiscible front is stabilized by interfacial tension when the front radius is small but becomes unstable as the front radius grows larger. When the thermal front is unstable, it destabilizes the immiscible fluid front and makes instability possible at smaller front radii. When the thermal front is stable, it stabilizes the fluid front and delays the growth of instabilities. However, the thermal front has only a small impact on the maximum obtainable perturbation growth rates when the front radius is large. In porous medium flow we observe that a thermal front that lags further behind the fluid front is more effective at stabilizing the fluid front.

DOI: 10.1103/PhysRevE.97.063112

I. INTRODUCTION

When an injected fluid is used to displace another in a porous medium or Hele-Shaw cell and the injected fluid has the lower viscosity, it is possible for the interface separating the two fluids to become unstable. This instability, commonly referred to as viscous fingering, was first described by Hill [1] in a series of displacement experiments using a column packed with charcoal. The same stability problem was later expanded on in several studies considering immiscible linear displacement [2,3] and radial displacement [4,5]. In these studies of immiscible displacement, interfacial tension was found to have a stabilizing influence. Viscous fingering also occurs in miscible displacement, which was first studied in detail by Tan and Homsy [6] for rectilinear flow and Tan and Homsy [7] for radial flow. A review of the viscous fingering literature was written by Homsy [8] for both miscible and immiscible displacement in porous media and Hele-Shaw cells.

If the fluid injected into the porous medium has a different temperature, a coupled two-front stability problem emerges. Because the heat is shared with the porous matrix, a second thermal front lagging behind the fluid front travels through the porous medium. Since the viscosity changes with temperature, fingering instabilities can occur on both fronts. This particular problem was studied, using linear stability theory for radial miscible displacement, by Pritchard [9]. The stability of the overall system was found to be dominated by the fluid front, which had a much lower diffusivity than the thermal front. The thermal front, however, still had an impact on the growth rates of perturbations.

Several studies, both using linear stability theory and numerical simulations, have looked into this type of thermoviscous stability problem in miscible displacement, including studies of linear displacement [10,11] and the quarter five-spot [12]. Although far less attention has been paid to the immiscible thermoviscous stability problem, a recent numerical study [13] investigated the effect of different injection temperatures in immiscible displacement. It was found that the fluid interface was stabilized by a cold injection fluid and destabilized by a warm injection fluid. Once the fingers started forming, however, the temperature had little impact on the growth. This type of two-front stability problem also shares similarities with the double interface problem studied by Cardoso and Woods [14], where the injected fluid was displacing a second and third fluid. Some important similarities are the interaction between two fronts separated in space and the stabilizing influence of interfacial tension. However, the problem studied by Cardoso and Woods [14] also differs in that both fronts are nondiffusive and stabilized by interfacial tension.

We use linear stability theory to study the coupled stability problem that occurs when a fluid is injected into a porous medium or Hele-Shaw cell saturated with a fluid of different viscosity and temperature. We consider immiscible displacement and investigate how the diffusion-stabilized thermal front impacts the stability of the immiscible fluid front stabilized by interfacial tension. In the Hele-Shaw cell the two fronts are colocated, while in the porous medium the thermal front lags behind. This thermoviscous stability problem is interesting in itself, as a coupled dual front stability problem, but is also of relevance in enhanced oil recovery [15], where hot water injection is sometimes used to displace oil.

The mathematical formulation of the physical problem is described in Sec. II, and the linear stability analysis is presented in Sec. III. Results for the stability problem are plotted and discussed in Sec. IV A for Hele-Shaw flow and Sec. IV B for porous medium flow. The main results and conclusions are summarized in Sec. V.

II. PROBLEM FORMULATION

We consider the radial displacement flow that results from a point source injection at the origin in a two-dimensional plane, describing a two-dimensional porous medium or a Hele-Shaw

*research@christophernilsen.no

cell. The plane is initially filled with fluid 2 with viscosity $\hat{\mu}_\infty$ and temperature $\hat{T}_\infty$. At time $\hat{t} = 0$ fluid 1 with temperature $\hat{T}_0$ and viscosity $\hat{\mu}_0$ is injected at constant areal flux $\hat{q}$, which gives a volume flux $\hat{q}/\hat{h}$ for a Hele-Shaw cell with plate spacing $\hat{h}$. A front separating fluid 1 from fluid 2 at $\hat{r} = \sqrt{\hat{q}\hat{t}/\pi}$ moves through the medium. The velocity $\hat{\boldsymbol{u}} = (\hat{u}_r, \hat{u}_\theta)$ in fluid j is $\hat{\boldsymbol{u}}_j$, the pressure is $\hat{p}_j$ and the temperature is $\hat{T}_j$. When writing equations that are satisfied in both fluids 1 and 2, we drop the index for simplicity.

The velocity $\hat{\boldsymbol{u}}$, pressure $\hat{p}$, and temperature $\hat{T}$ are governed by the equation for mass conservation,

$$\hat{\nabla} \cdot \hat{\boldsymbol{u}} = 0, \tag{1}$$

Darcy's law,

$$\hat{\nabla} \hat{p} = -\frac{\hat{\mu}}{\hat{k}} \hat{\boldsymbol{u}}, \tag{2}$$

and the advection diffusion equation for temperature,

$$\frac{\partial \hat{T}}{\partial \hat{t}} + \frac{\lambda}{\phi} \hat{\nabla} \cdot (\hat{\boldsymbol{u}} \hat{T}) = \hat{\kappa}_T \hat{\nabla}^2 \hat{T}, \tag{3}$$

where $\hat{\kappa}_T$ is the thermal diffusivity. In porous medium flow $\hat{k}$ is the permeability of the porous matrix, while in Hele-Shaw flow it is equal to $\hat{h}^2/12$.

The thermal lag coefficient λ [9,16] in porous medium flow is defined as

$$\lambda = \frac{\phi_t \hat{\rho}_{\text{fluid}} \hat{C}_{\text{fluid}}}{\phi_t \hat{\rho}_{\text{fluid}} \hat{C}_{\text{fluid}} + (1 - \phi_t) \hat{\rho}_{\text{matrix}} \hat{C}_{\text{matrix}}} < 1, \tag{4}$$

with density $\hat{\rho}$ and specific heat capacity $\hat{C}$. The total porosity ϕ_t is different from the effective porosity ϕ, which is associated with connected void space. While the viscosity $\hat{\mu}$ is a function of temperature and different in the two fluids, all other parameters are constant and equal in the two fluids.

The thermal lag coefficient is a measure of how much the thermal front lags behind the fluid front, as a result of sharing heat with the porous matrix. By representing the heat loss from the fluid using the thermal lag coefficient we assume that the fluid is in thermal equilibrium with the matrix. For simplicity, we assume that there is no heat loss through the upper and lower boundaries of the Hele-Shaw cell. This allows us to use the same formulation for heat transfer as in the porous medium flow but with $\lambda = 1$. Throughout this paper we refer to the thermal and fluid fronts as two separate fronts, even when $\lambda = 1$ and they are colocated.

We choose an arbitrary lengthscale $\hat{r}_0$, define the timescale $\hat{t}_0 = 2\pi \hat{r}_0^2/\hat{q}$, and nondimensionalize the equations using

$$r = \frac{\hat{r}}{\hat{r}_0}, \quad t = \frac{\hat{t}}{\hat{t}_0}, \quad u_{r,\theta} = \hat{u}_{r,\theta} \frac{\hat{t}_0}{\hat{r}_0 \phi},$$
$$T = \frac{\hat{T} - \hat{T}_0}{\hat{T}_\infty - \hat{T}_0}, \quad \mu = \frac{\hat{\mu}}{\hat{\mu}_0}, \quad p = \hat{p} \frac{2\pi \hat{k}}{\hat{\mu}_0 \phi \hat{q}}. \tag{5}$$

The nondimensional governing equations in fluids 1 and 2 are

$$\frac{1}{r} \frac{\partial}{\partial r}(r u_r) + \frac{1}{r} \frac{\partial u_\theta}{\partial \theta} = 0, \tag{6}$$

$$\frac{\partial p}{\partial r} = -\mu u_r, \quad \frac{1}{r} \frac{\partial p}{\partial \theta} = -\mu u_\theta, \tag{7}$$

and

$$\frac{\partial T}{\partial t} + \lambda \left[\frac{1}{r} \frac{\partial (r u_r T)}{\partial r} + \frac{1}{r} \frac{\partial (u_\theta T)}{\partial \theta} \right] = \frac{1}{\text{Pe}} \left[\frac{1}{r} \frac{\partial}{\partial r} \left(r \frac{\partial T}{\partial r} \right) + \frac{1}{r^2} \frac{\partial^2 T}{\partial \theta^2} \right], \tag{8}$$

where $\text{Pe} = \hat{q}/(2\pi \hat{\kappa}_T)$ is the Péclet number.

Following Tan and Homsy [7] we use an exponential dependence on temperature for the viscosity and specify the viscosities in fluids 1 and 2 as

$$\mu_1 = e^{-\beta T}, \quad \mu_2 = \alpha e^{-\beta T}. \tag{9}$$

The parameters α and β decide the change in viscosity over the fluid and thermal fronts, respectively. Because the temperature is normalized to take values between 0 and 1, a change in β can be interpreted either as a change in the temperature sensitivity of the viscosity or as a change in the temperature itself. Negative values of β lead to an increase in viscosity over the thermal front (from behind to in front of) and therefore a potentially unstable thermal front. When β is positive the thermal front is stable.

It is important to remember that even though $\beta < 0$ means that the viscosity μ is increasing with increased T it does not necessarily mean that the viscosity is increasing with increased $\hat{T}$. Because of the chosen nondimensionalization of $\hat{T}$ [Eq. (5)], the viscosity will decrease with increasing $\hat{T}$ when $\beta < 0$ if $\hat{T}_0 > \hat{T}_\infty$. For a fluid with a viscosity that decreases with an increase in $\hat{T}$, the two cases $\beta < 0$ and $\beta > 0$ correspond with $\hat{T}_0 > \hat{T}_\infty$ and $\hat{T}_0 < \hat{T}_\infty$, respectively. The two different cases studied are therefore best understood as hot fluid injection ($\beta < 0$) and cold fluid injection ($\beta > 0$).

The solution to the governing equations must satisfy the boundary conditions

$$T = 0 \quad \text{at} \quad r = 0, \quad T \to 1 \quad \text{as} \quad r \to \infty, \quad \lim_{r \to 0} r u_r = 1, \tag{10}$$

along with matching conditions at the interface between fluid 1 and 2 that we will get back to in Sec. III. By using the similarity variable $\zeta = r^2/(4t)$, we find the base temperature solution independent of θ as

$$T_b(r,t) = \frac{\gamma(\lambda \text{Pe}/2, \text{Pe}\zeta)}{\Gamma(\lambda \text{Pe}/2)}, \tag{11}$$

where $\Gamma(s)$ is the standard γ function and $\gamma(s,x)$ is the lower incomplete γ function.

The base viscosity $\mu_b = \mu(T_b)$ is plotted in Fig. 1 for three different values of λ to illustrate how the thermal lag coefficient influences the position of the thermal front. The thermal front is the diffuse region where the viscosity changes as a result of the change in temperature. As seen in Fig. 1 this thermal front partly overlaps with the fluid interface, and the extent to which it overlaps depends on λ and Pe. We choose to define the position of the thermal front as $\sqrt{\lambda \hat{q} \hat{t}/\pi}$, which is the radius at which the temperature change occurs if $\text{Pe} \to \infty$. This is the same definition of the thermal front position as that used by Pritchard [9].

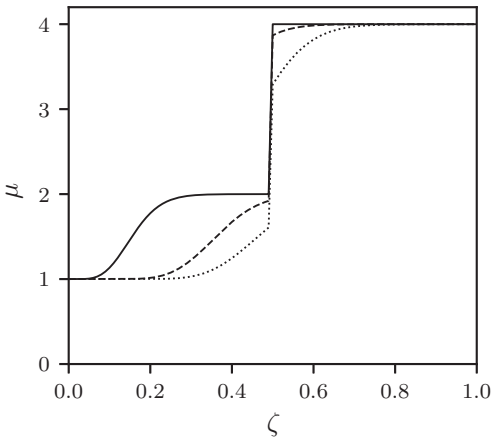

FIG. 1. Base viscosity solution for Pe = 50, $\alpha = 2$, $\beta = -\log 2$, and $\lambda = 0.3$ (solid line), 0.7 (dashed line) and 0.9 (dotted line).

III. THERMOVISCOUS STABILITY ANALYSIS

The nondimensional system of equations in Sec. II describes a physical system in which we have a moving fluid front at $R(t) = \sqrt{2t}$ and a second thermal front at $R_T(t) = \sqrt{2\lambda t}$. We perturb the fluid interface at $R(t)$ such that the fluid fluid interface is located at $r = R(t) + \epsilon e^{im\theta} a(t)$, and we expand the velocity, temperature, and pressure in the following way:

$$u_r = u_{rb} + \epsilon e^{im\theta} U(r,t), \quad u_\theta = \epsilon e^{im\theta} V(r,t),$$
$$T = T_b + \epsilon e^{im\theta} T(r,t), \quad p = p_b + \epsilon e^{im\theta} P(r,t). \quad (12)$$

The viscosity then becomes

$$\mu = \mu_b - \beta \mu \epsilon e^{im\theta} T, \quad (13)$$

with μ_b given by Eq. (9) evaluated with temperature T_b. By solving for the perturbations U, V, T, P, and a, we determine the spatial and temporal evolution of the first order perturbations. The solution for the interface perturbation a will tell us if a mode m perturbation grows or decays, and therefore if the interface is stable or unstable. Figure 2 shows a sketch of the two fronts and the wavelike perturbations.

Inserting the first-order expansions into the governing equations, and eliminating P and V, we get to first order

$$\frac{\partial}{\partial r}\left[\mu_b r \frac{\partial}{\partial r}(rU)\right] = \frac{m^2}{r}(Ur - \beta T)\mu_b, \quad (14)$$

and for the temperature

$$\frac{\partial T}{\partial t} + \lambda\left(U\frac{\partial T_b}{\partial r} + \frac{1}{r}\frac{\partial T}{\partial r}\right) = \frac{1}{\mathrm{Pe}}\left[\frac{1}{r}\frac{\partial}{\partial r}\left(r\frac{\partial T}{\partial r}\right) - \frac{m^2}{r^2}T\right]. \quad (15)$$

By introducing $\chi = rU$ and $\zeta = r^2/(4t)$, the equations can be written as

$$\frac{\partial}{\partial \zeta}\left(\mu_b \zeta \frac{\partial \chi}{\partial \zeta}\right) = \frac{m^2}{4\zeta}(\chi - \beta T)\mu_b, \quad (16)$$

$$t\frac{\partial T}{\partial t} = \frac{1}{\mathrm{Pe}}\frac{\partial}{\partial \zeta}\left(\zeta\frac{\partial T}{\partial \zeta}\right) + \left(\zeta - \frac{\lambda}{2}\right)\frac{\partial T}{\partial \zeta} - \frac{1}{4}\frac{m^2}{\mathrm{Pe}}\frac{T}{\zeta} - \frac{\lambda}{2}\chi\frac{\partial T_b}{\partial \zeta}. \quad (17)$$

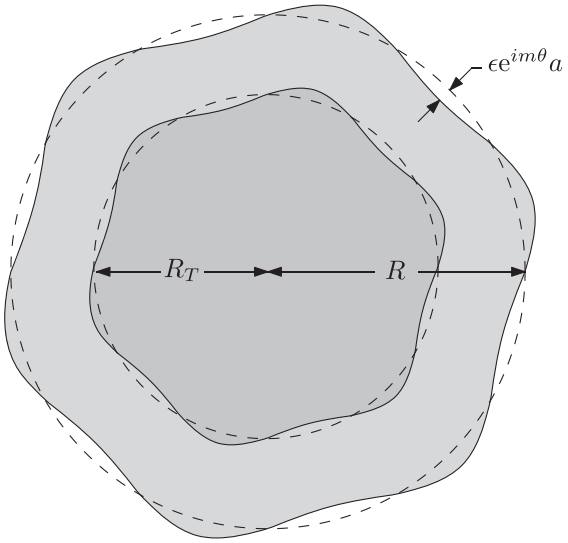

FIG. 2. Circular fluid interface of radius R with perturbation $\epsilon e^{im\theta} a$, and position of diffuse thermal front at R_T.

The perturbations must vanish far away from the interface and therefore we have the boundary conditions

$$T, \chi = 0 \quad \text{at} \quad \zeta = 0 \quad \text{and as} \quad \zeta \to \infty. \quad (18)$$

At the interface ($\zeta = 1/2$) we have the matching conditions

$$\chi_1\left(\tfrac{1}{2},t\right) = \chi_2\left(\tfrac{1}{2},t\right), \quad T_1\left(\tfrac{1}{2},t\right) = T_2\left(\tfrac{1}{2},t\right), \quad (19)$$

and

$$\left.\frac{\partial T_1}{\partial \zeta}\right|_{\zeta=\frac{1}{2}} = \left.\frac{\partial T_2}{\partial \zeta}\right|_{\zeta=\frac{1}{2}}. \quad (20)$$

The final matching condition is associated with the pressure jump over the immiscible interface. We follow Chuoke *et al.* [2] and Paterson [5] and assume that the pressure difference is equal to the product of interfacial tension $\hat{\sigma}$ and the macroscopic curvature of the perturbed interface. This gives us the last matching condition

$$\left.\frac{\partial \chi_1}{\partial \zeta}\right|_{\zeta=\frac{1}{2}} - \alpha \left.\frac{\partial \chi_2}{\partial \zeta}\right|_{\zeta=\frac{1}{2}} = m^2 a\left[\frac{\alpha - 1}{\sqrt{2t}} + \frac{\sigma(1-m^2)}{e^{-\beta T_b(1/2)}}\right]. \quad (21)$$

The nondimensional interfacial tension is defined as $\sigma = 2\pi\hat{k}\hat{\sigma}/(\hat{q}\hat{r}_0\hat{\mu}_0)$.

The temperature and velocity equations are through these interface conditions coupled with the equation for the interface perturbation a:

$$t\frac{da}{dt} + \frac{a}{2} = \sqrt{\frac{t}{2}}\chi_1\left(\frac{1}{2},t\right). \quad (22)$$

Equations (16), (17), and (22) are solved numerically by discretizing in the ζ coordinate using a spectral element formulation and integrating in time. Details of the numerical methodology are given in the Appendix.

IV. RESULTS

A. Hele-Shaw flow ($\lambda = 1$)

1. Neutrally stable thermal front ($\beta = 0$)

Before we go into the thermoviscous stability results, we will briefly look at some features of the single front radial stability solution obtained when $\beta = 0$. For a single radial front moving as $R(t) = \sqrt{2t}$, the perturbation amplitude a follows [5]

$$\frac{1}{a}\frac{da}{dt} = \frac{1}{2t}\left(m\frac{\mu_2 - \mu_1}{\mu_1 + \mu_2} - 1\right) - \frac{\sigma}{(2t)^{3/2}}\frac{m(m^2-1)}{\mu_1 + \mu_2}. \quad (23)$$

With initial perturbation $a(t_0) = 1$, the solution is

$$a(t) = \left(\frac{t}{t_0}\right)^{\frac{1}{2}(m\frac{\mu_2-\mu_1}{\mu_1+\mu_2}-1)} \times \exp\left[\frac{\sigma}{2^{1/2}}\frac{m(m^2-1)}{\mu_1+\mu_2}(t^{-1/2} - t_0^{-1/2})\right]. \quad (24)$$

When $t \to \infty$ $a(t)$ grows as a power law with exponent

$$\omega_\infty = \frac{1}{2}\left(m\frac{\mu_2 - \mu_1}{\mu_1 + \mu_2} - 1\right). \quad (25)$$

With the nondimensional viscosity defined in Eq. (9), we get $\mu_1 = 1$ and $\mu_2 = \alpha$. This is the same problem as the one studied by Paterson [5], although the general solution in Eq. (24) was not included there. All results presented in this paper where $\beta = 0$ are from Eq. (24) and not from numerical simulations.

As long as the interfacial tension σ is not equal to zero, the only effect of changing it is to rescale time. This is true both for the simple one front solution in Eq. (24) and the complete thermoviscous stability problem. Therefore all simulations with nonzero σ use $\sigma = 1$, and the results are plotted as functions of the scaled time t/σ^2. Time is linked to the radius of the moving front through $R(t) = \sqrt{2t}$, and the limit $t/\sigma^2 \to \infty$ is also the large radius limit $R/\sigma \to \infty$.

The single front solution in Eq. (24) is plotted in Fig. 3 for three different values of m, and with $\mu_2 = \alpha = 4$. For low values of t/σ^2 the front is stabilized by the interfacial tension and the perturbation magnitude falls rapidly. Then we

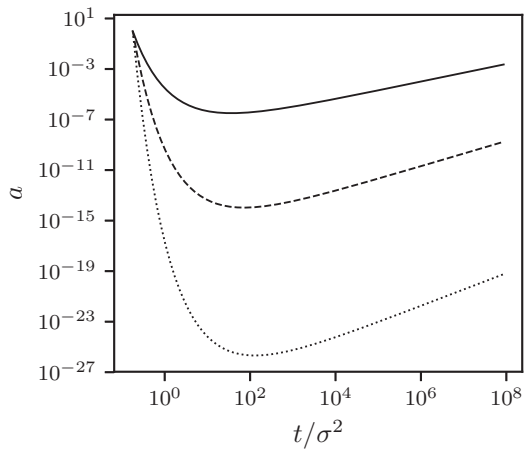

FIG. 3. Perturbation amplitude a as function of t/σ^2 for $m = 4$ (solid line), 5 (dashed line), and 6 (dotted line).

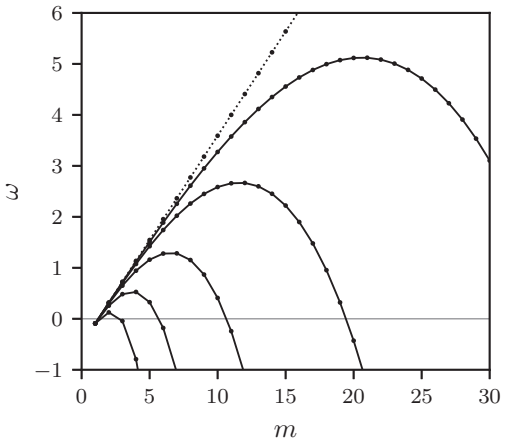

FIG. 4. Perturbation growth rate ω as function of m at times $t/\sigma^2 = 1, 10, 10^2, 10^3$ and 10^4 (solid lines from left to right at $\omega = -1$) compared with perturbation growth as $t/\sigma^2 \to \infty$ (dotted line).

get to a point where the destabilizing effect of the viscosity difference overcomes the stabilizing effect of the interfacial tension and the perturbation starts growing. As time increases the curvature of the perturbation decreases, and the relative importance of interfacial tension decreases. Higher wave-number perturbations will decay more rapidly initially and start growing at a later time, but grow more rapidly when they first become unstable. This is seen in Fig. 3.

As a measure of how fast a perturbation grows at a given time we use the perturbation growth rate,

$$\omega = \frac{t}{a}\frac{da}{dt}. \quad (26)$$

When the perturbation grows as a power law, which it does when $t/\sigma^2 \to \infty$, ω is the exponent of that power law. If $\omega > 0$, then perturbations grow in amplitude and the flow is unstable. However, the radius of the front grows with $\omega = 1/2$ and so for the perturbation to grow in size relative to the front size, ω must be greater than $1/2$.

In Fig. 4 we plot the growth rate ω at different times when $\mu_2 = \alpha = 10$. The dots represent the actual data points, while the lines are added to make the plot easier to read. When $t/\sigma^2 \to \infty$, ω approaches ω_∞, which is also plotted in Fig. 4. We can see that the first mode to become unstable is the $m = 2$ mode, and that the higher order modes are effectively stabilized by interfacial tension. After this, higher wave-number modes become unstable as time, and the diameter of the front, increases. The most unstable mode (highest ω) also moves to higher and higher values of m, as the growth rate asymptotically approaches the $t/\sigma^2 \to \infty$ solution.

2. Stable or unstable thermal front ($\beta < 0$ or $\beta > 0$)

When $t/\sigma^2 \to \infty$, the interfacial tension has no impact and a approaches power-law growth, i.e., ω approaches a constant value. The asymptotic values of ω are obtained by doing simulations with $\sigma = 0$ and comparing with the isothermal ($\beta = 0$) growth rates (ω_∞) in Fig. 5. The Péclet number is 50, $\alpha = 10$, and $\beta = -\log 1000$, 0, and $\log 1000$.

The effect of the thermal front on the stability of the interface is moderate, even when the viscosity ratio is 100 times greater

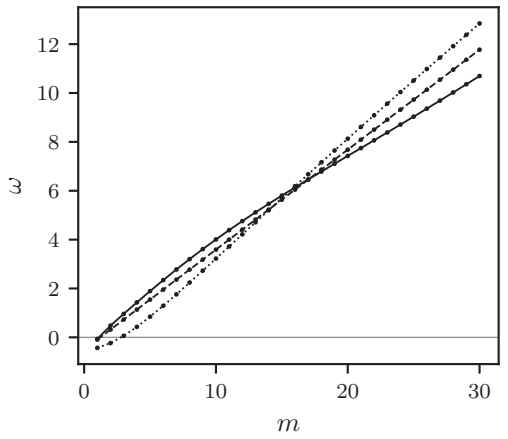

FIG. 5. Growth rate as function of m as $t/\sigma^2 \to \infty$ for Hele-Shaw flow with $\alpha = 10$ and $\beta = -\log 1000$ (solid line), 0 (dashed line), and $\log 1000$ (dotted line).

over the thermal front. It is clear that the growth rate of the interface is dominated by the immiscible front, when it is not stabilized by interfacial tension. When $\beta = -\log 1000$, the temperature has a small destabilizing effect at small wave numbers and a stabilizing effect at high wave numbers. The thermal front with $\beta = \log 1000$ has a stabilizing effect at small wave numbers and a destabilizing effect at high wave numbers. If Pe is reduced, the crossover point moves to lower values of m, while an increase in Pe shifts the crossover point towards higher m (not shown).

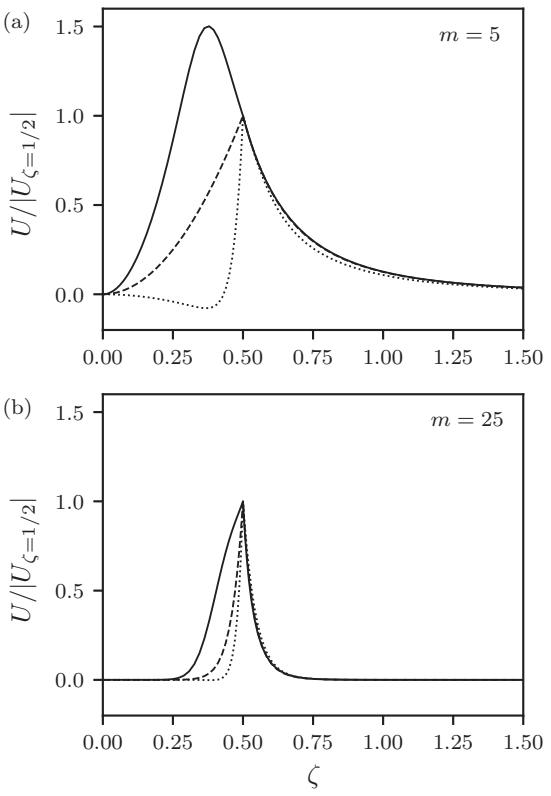

FIG. 6. Radial velocity perturbation in the $t/\sigma^2 \to \infty$ case with $\alpha = 10$, and $\beta = -\log 1000$ (solid line), 0 (dashed line), and $\log 1000$ (dotted line).

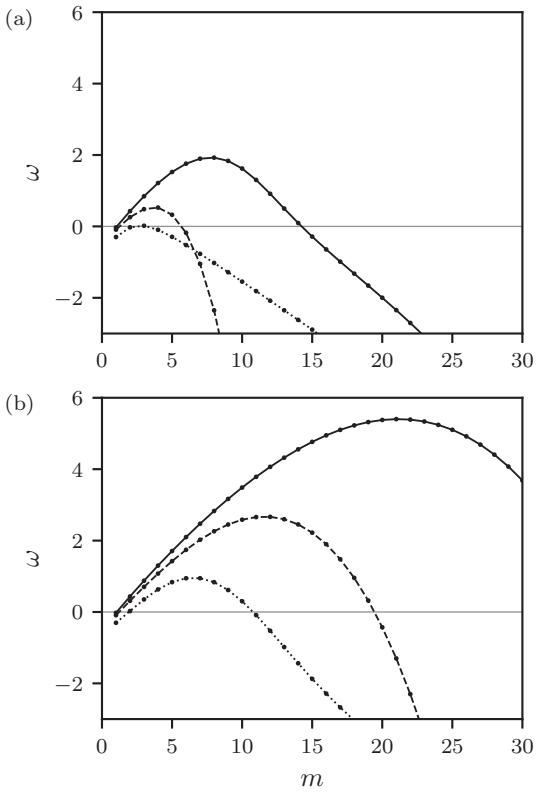

FIG. 7. Perturbation growth rate as function of m for $\alpha = 10$ and $\beta = -\log 10$ (solid line) $\beta = 0$ (dashed line) and $\beta = \log 10$ (dotted line). The time is $t/\sigma^2 = 10$ in (a) and 100 in (b).

The effect at low wave numbers is consistent with what we would expect for thermal fronts with unstable ($\beta < 0$) and stable ($\beta > 0$) viscosity profiles. To understand the reversal at high wave numbers, we plot the radial perturbation velocity U in Fig. 6. Considering the moderate effect of the thermal front on the growth rates in Fig. 5, the strong effect on the shape of the radial velocity perturbation is noteworthy.

When $m = 5$, the destabilizing effect of the temperature is creating a velocity maximum behind the fluid interface that dominates the shape of the velocity. The much higher viscosity jump ($\beta = -\log 1000$) caused by the change in temperature, makes the diffuse thermal front more unstable than the fluid front. When $\beta = \log 1000$, the stabilizing effect of the temperature induced viscosity profile creates a set of counter-rotating vortices behind the fluid front, as seen by the negative values of U at low ζ when $m = 5$ and $\beta = \log 1000$. These counter-rotating vortices reduce the growth rate of the fluid front.

At $m = 25$ the effect of temperature is smaller and the impact on the growth rates is different. When $\beta = -\log 1000$ and the wave number is high, the unstable thermal front is partly stabilized by diffusion. This has a strong impact on how it is able to modify the stability of the fluid interface. At $m = 25$ the growth rate of the thermal front is much lower than the growth rate of the fluid front even though the velocity jump is much greater over the thermal front. This is because of the strong damping effect of diffusion at higher wave numbers, and the less unstable thermal front is impeding the growth of the fluid front.

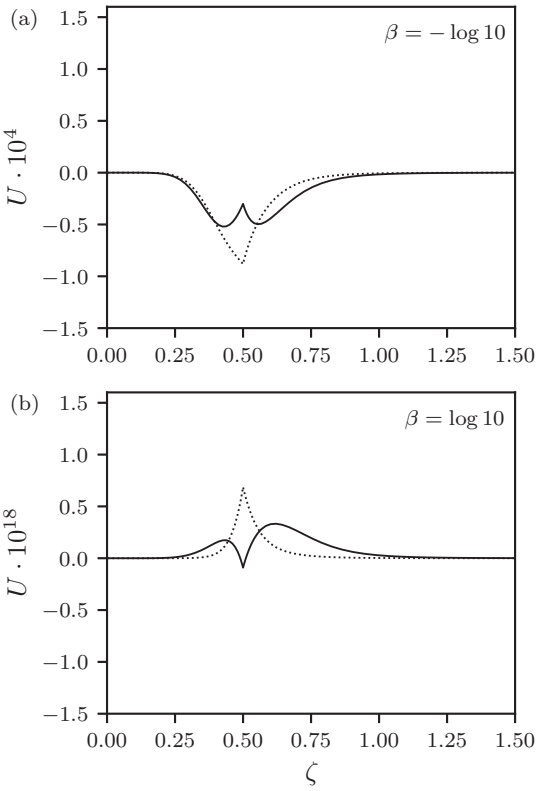

FIG. 8. Radial velocity perturbation for (a) $t/\sigma^2 = 18.28$ (solid line) and $t/\sigma^2 = 49.68$ (dotted line), and (b) $t/\sigma^2 = 2713$ (solid line) and $t/\sigma^2 = 7374$ (dotted line), for $m = 15$.

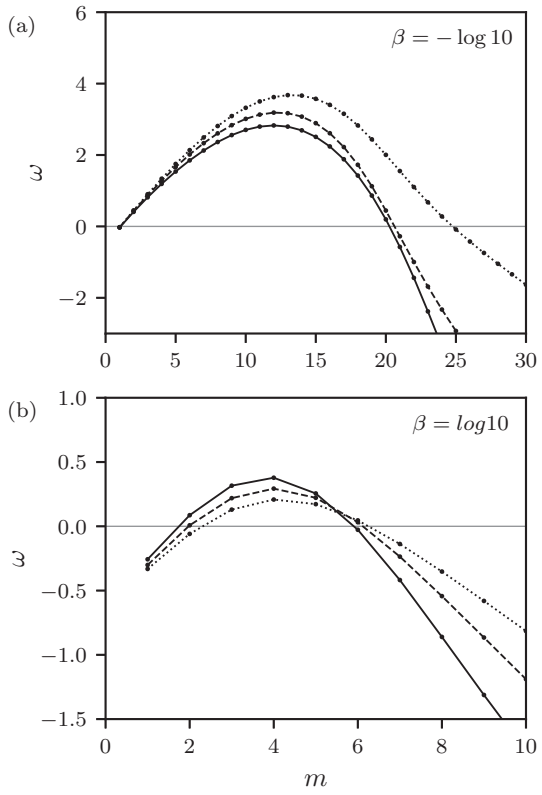

FIG. 9. Perturbation growth rate at time $t/\sigma^2 = 100$ for Pe $= 25$ (solid line), Pe $= 50$ (dashed line) and Pe $= 100$ (dotted line).

When $\beta = \log 1000$ and the thermal front has a stable viscosity ratio, the growth rate of the fluid interface is increased, and not decreased as one might expect. Looking at the velocity profile in Fig. 6(b), we see that the stabilizing counter-rotating vortices have been damped by diffusion, and what remains is a sharper and more unstable fluid perturbation. It has previously [17] been shown that diffusion can have a destabilizing effect in miscible displacement when the viscosity profile is nonmonotonic.

After having looked at what happens when the radius of the front is large, or $t/\sigma^2 \to \infty$, we will consider the effects of finite interfacial tension ($\sigma = 1$). In Fig. 7 the perturbation growth rates are plotted at two different times and for the three different thermal stability cases, $\beta < 0$, $\beta = 0$, and $\beta > 0$. We use $\alpha = 10$, and because the effect of the thermal front is much more significant than in the $t/\sigma^2 \to \infty$ case, we use $\beta = \pm \log 10$. The Péclet number is still 50.

At both $t/\sigma^2 = 10$ and 100, we see that the thermal front with $\beta = -\log 10$ dramatically increases the growth rate of the perturbation while also shifting the most unstable mode towards higher values of m. Since the growth rates obtained as $t/\sigma^2 \to \infty$ will not be much changed by the thermal front with $\beta = -\log 10$, the primary effect of the unstable thermal front is to shift the point at which the perturbations start growing to earlier times or smaller front radii. At all times, the unstable thermal front will make the fluid front more unstable and increase the frequency of the most unstable perturbation.

When $\beta = \log 10$, the front is stabilized. The growth rate is decreased and the most unstable mode is shifted to lower m. Another worthwhile observation is that when $\omega < 0$ in Fig. 7(a), the perturbations decay much faster when $\beta = 0$ than when $\beta = \pm \log 10$. This is because the diffusive dampening of the temperature perturbation is much slower than the dampening caused by interfacial tension, and so even the stable thermal front will impede the decay of the fluid front. The results shown in Figs. 5 and 7 are consistent with the observations made by Jackson *et al.* [13] that temperature could stabilize or destabilize the fluid interface, but once the interface becomes unstable its growth rates are not much influenced by temperature.

The corresponding velocity perturbation profiles for $m = 15$ are plotted in Fig. 8 right before and right after ω goes from negative to positive. Both when $\beta = -\log 10$ and when $\beta = \log 10$ we see that the thermal and fluid fronts are working against each other before the growth rate becomes positive. The unstable thermal front ($\beta = -\log 10$) is destabilizing the fluid front before it is on its own unstable and therefore expediting the growth of instabilities on the interface. The stable thermal front is holding back an unstable fluid front and therefore delaying the destabilisation of the interface.

For all the results thus far, the Péclet number (Pe) has been 50. To illustrate the effect of different values of Pe, we plot the growth rates for Pe $= 25$, 50, and 100 in Fig. 9, with $\alpha = 10$ and $\beta = \pm \log 10$. When $\beta = -\log 10$, the growth rates increase with increasing Pe. This is due to the reduced dampening effect of diffusion at higher Péclet numbers. Since the unstable thermal front is stabilized by diffusion, a reduction in diffusion naturally leads to a more unstable interface.

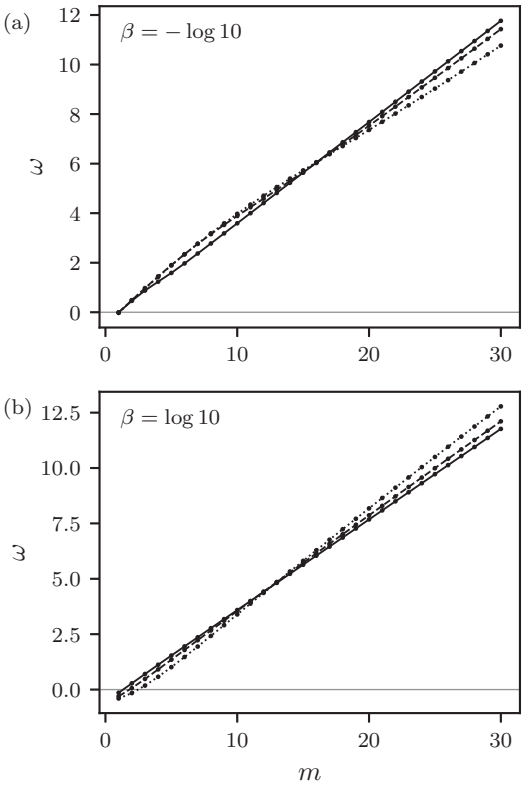

FIG. 10. Growth rate as function of m as $t/\sigma^2 \to \infty$ for porous medium flow with $\alpha = 10$ and $\lambda = 0.3$ (solid line), 0.7 (dashed line), and 0.9 (dotted line), for (a) $\beta = -\log 1000$ and (b) $\beta = \log 1000$.

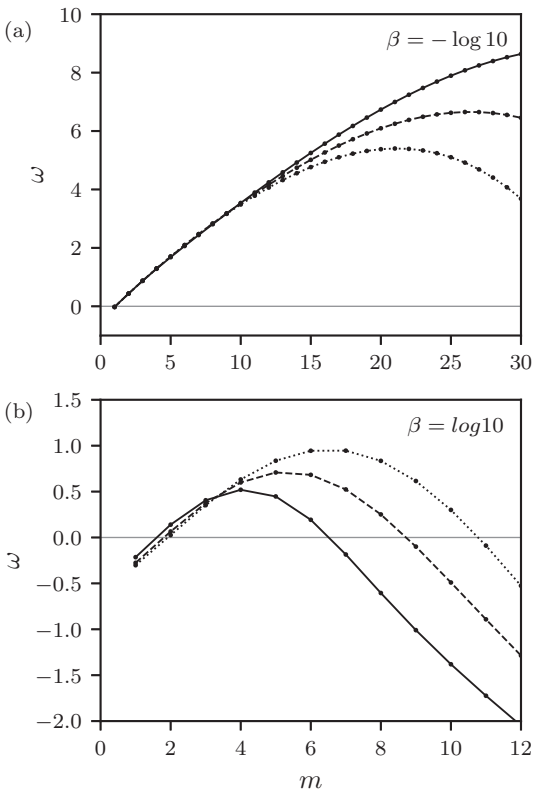

FIG. 11. Perturbation growth rate at $t/\sigma^2 = 1000$ in porous medium flow with $\lambda = 0.7$ (solid line) and $\lambda = 0.9$ (dashed line) compared with Hele-Shaw flow with $\lambda = 1$ (dotted line).

When $\beta = \log 10$ the stable higher wave-number modes decay faster when Pe is increased. For these wave numbers the diffuse thermal front is having a dampening effect and increased diffusion leads to quicker decay. At lower values of m, when ω is greater than zero, an increase in Pe reduces the growth rate of the front. Even when $\lambda = 1$, most of the change in viscosity caused by temperature happens behind the fluid front. When Pe is reduced, there is less overlap between the viscosity jump caused by the temperature change and the viscosity jump between the two fluids. Why this might make the thermal front more effective at stabilizing the fluid front is discussed in Sec. IV B.

B. Porous medium flow ($\lambda < 1$)

We have so far looked into results for Hele-Shaw flow, when $\lambda = 1$. In a porous medium, where $\lambda < 1$, the thermal front will lag behind the fluid front and we expect this to change how it influences the stability. Nevertheless, the observations made in Sec. IV A about how the thermal front impacts the stability are also seen in porous medium flows. When $\beta < 0$, the unstable thermal front will make instability possible at earlier times (lower t/σ^2), or lower front radii. When $\beta > 0$, the opposite is true. However, there are also some differences, which will be made clear in the following results. We use $\mathrm{Pe} = 50$ throughout this section.

In Fig. 10 we investigate the effect of the thermal lag coefficient λ, by revisiting what happens when interfacial tension becomes insignificant ($t/\sigma^2 \to \infty$). The effect of the thermal front on instability is similar to what was seen in Fig. 5, with the difference that the effect becomes less pronounced as λ is reduced. When $\lambda = 0.9$ and the fronts are strongly coupled, the stabilizing and destabilizing effect is much the same as in Hele-Shaw flow. When $\lambda = 0.3$, the temperature has almost no effect on stability.

A lower value of λ means the thermal and fluid fronts are more separated in space, which reduces the thermal fronts ability to influence the stability of the fluid front. This is very much in line with both reasonable expectations for two interacting fronts and previous results for two diffusive fronts [9].

Once again this is changed when interfacial tension is introduced. The perturbation growth rates for the porous medium flow with $\lambda = 0.7$, $\alpha = 10$, and $\beta = \pm \log 10$ are plotted in Fig. 11, while the corresponding velocity perturbation profiles, right before and right after the front becomes unstable, are plotted in Fig. 12. When $\beta = -\log 10$ and the thermal front is unstable, the effect of temperature is to increase the growth rates and shift the most unstable mode to higher m. This effect is made stronger, not weaker, by a reduction in λ, as seen in Fig. 11. Looking at the velocity profile in Fig. 12(a), we see that before the perturbation starts growing the profile is completely dominated by the unstable thermal front. When the thermal front is further behind the fluid front it is less limited by the stabilizing influence of the interfacial tension and therefore ends up being more unstable. This leads to perturbations on the fluid front growing sooner, than in the Hele-Shaw flow.

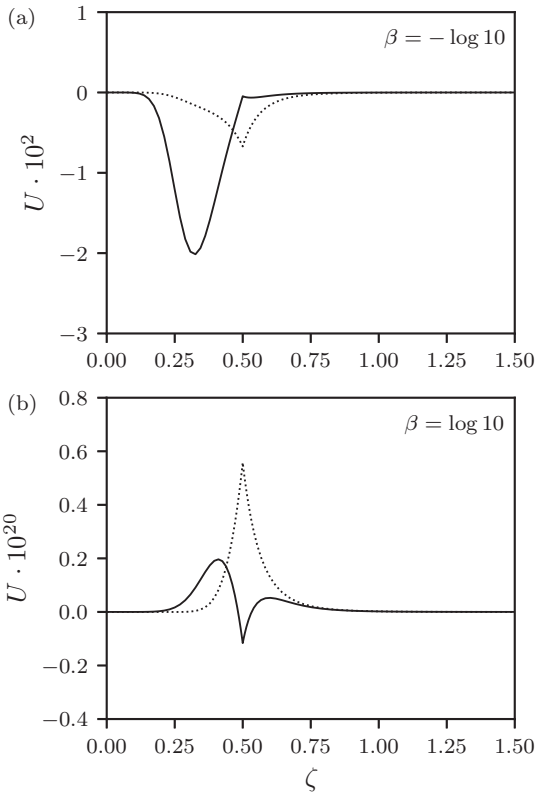

FIG. 12. Radial velocity perturbation in porous medium flow with $\lambda = 0.7$ and $m = 15$ for (a) $t/\sigma^2 = 2.474$ (solid line) and 18.28 (dotted line), and (b) $t/\sigma^2 = 20\,040$ (solid line) and 54 490 (dotted line).

Lower values of λ (0.5 and 0.3 were tested) resulted in growth rates very close to those found for $\lambda = 0.7$.

When $\beta = \log 10$ the thermal front is more effective in dampening the growth of the fluid front when λ is reduced, except at the lowest wave numbers. It is not obvious why the thermal front would be able to stabilize the fluid front more effectively when it lags further behind, but we propose a possible explanation. When λ is close to 1, the two fronts are overlapping and behave as one front with a nonmonotonic viscosity profile. The stability of this nonmonotonic viscosity profile will be largely determined by the sharp fluid front, but modified by the thermal viscosity profile. When the thermal front is further behind the fluid front it behaves more like a separate and stable front than as part of a combined nonmonotonic unstable viscosity front. The thermal front therefore remains more stable and creates an effective barrier to perturbation growth behind the fluid front. This also accounts for the effect of Pe seen in Fig. 9, where the thermal front was more effective at stabilizing the fluid front when there was less overlap between the two.

V. CONCLUSION

We have investigated the thermoviscous stability problem that results when fluid is injected at a constant flowrate from a point source in a Hele-Shaw cell or two-dimensional porous medium. When the temperature and base viscosity of the injected fluid differs from the fluid initially saturating the plane, we get a coupled two-front stability problem where both the thermal and fluid fronts contribute to the overall stability. We have used linear stability theory to determine how much the stability of the immiscible fluid front is impacted by the thermal front. The radial fluid front is effectively stabilized by interfacial tension if the radius is small, but becomes unstable at larger radii.

When $t/\sigma^2 \to \infty$ and the radius is large, interfacial tension has no stabilizing effect on the interface and the stability of the coupled problem is dominated by the unstable sharp fluid front. Only small changes to the perturbation growth rates are made by the thermal front and only when the viscosity jump over the thermal front is much greater than the viscosity jump over the fluid front. At finite radii, the thermal front can have a dramatic effect on the stability of the fluid interface by either advancing or delaying the transition to instability. If the thermal front is unstable, perturbations on the fluid interface start growing earlier and the most unstable mode is shifted to higher wave numbers. If the thermal front is stable, the opposite happens. These effects are seen in both Hele-Shaw and porous medium flow.

In porous medium flow the thermal front lags behind the fluid front by an amount determined by the thermal lag coefficient λ. At finite front radii, we find that the thermal front is more effective at stabilizing the unstable fluid front in porous media if it lags further behind. When the thermal front is more separated from the fluid front it is not so easily destabilized, and it functions as a more effective barrier to the growth of perturbations on the fluid front.

The linear stability results presented here are only valid when the perturbation amplitudes are small. To determine the extent to which the observations made here remain valid when the perturbations grow larger, fully nonlinear simulations would be a useful extension of the current work.

ACKNOWLEDGMENT

The project was funded by VISTA, a basic research program in collaboration between The Norwegian Academy of Science and Letters and Statoil.

APPENDIX: NUMERICAL METHODOLOGY

Equations (16), (17), and (22) are solved numerically as a coupled system. The equations are integrated in time using a third order backward differentiation formula (BDF), and discretized in the spatial direction by using a spectral element formulation. A nodal Nth order polynomial basis on the Gauss Lobatto Legendre points is used in each element.

The domain is divided into three elements, each with their own geometry transformation that transforms the reference variable $\xi \in (-1,1)$ to the physical domain, using the following functions:

$$\zeta^{(1)} = 0.25(1+\xi), \tag{A1}$$

$$\zeta^{(2)} = 0.5 + 1.1\frac{e^{0.7\xi} - e^{-0.7}}{e^{0.7} - e^{-0.7}}, \tag{A2}$$

$$\zeta^{(3)} = 2.0\frac{1+\xi}{1-\xi} + 1.6. \tag{A3}$$

The first element covers the part of the domain containing fluid 1, while the other two cover the rest. Element 3 stretches to infinity, where our boundary conditions are expressed. The constants in the geometry transformations are chosen so that the grid derivatives $\frac{d\zeta}{d\xi}, \frac{d\xi}{d\zeta}$ do not change much between adjoining elements. Continuity is enforced between element 2 and 3, while the matching conditions between element 1 and 2 are given by Eqs. (19), (20), and (21).

Before the equations are integrated in time, they are transformed to logarithmic time by introducing $\tau = \log t$. The third order BDF method is then used to integrate the equations in logarithmic time τ with the timestep $\Delta\tau$. By transforming to τ, more timesteps are used in the beginning of the simulation where the finest time resolution is needed, and the total error for a given number of timesteps is reduced.

We use $\Delta\tau = 10^{-4}$ and $N = 40$ for all simulations.

[1] S. Hill, Chem. Eng. Sci. **1**, 247 (1952).
[2] R. L. Chuoke, P. van Meurs, and C. van der Poel, Petrol. Trans. AIME **216**, 188 (1959).
[3] P. G. Saffman and G. Taylor, Proc. R. Soc. London **245**, 312 (1958).
[4] S. D. R. Wilson, J. Colloid Interface Sci. **51**, 532 (1975).
[5] L. Paterson, J. Fluid Mech. **113**, 513 (1981).
[6] C. T. Tan and G. M. Homsy, Phys. Fluids **29**, 3549 (1986).
[7] C. T. Tan and G. M. Homsy, Phys. Fluids **30**, 1239 (1988).
[8] G. M. Homsy, Annu. Rev. Fluid Mech. **19**, 271 (1987).
[9] D. Pritchard, J. Fluid Mech. **508**, 133 (2004).
[10] M. N. Islam and J. Azaiez, Transp. Porous Media **84**, 821 (2010).
[11] M. N. Islam and J. Azaiez, Transp. Porous Media **84**, 845 (2010).
[12] M. N. Islam and J. Azaiez, European J. Mech. B/Fluids **30**, 107 (2011).
[13] S. J. Jackson, H. Power, and D. Giddings, Comp. Fluids **156**, 621 (2017).
[14] S. S. S. Cardoso and A. W. Woods, J. Fluid Mech. **289**, 351 (1995).
[15] G. A. Pope, J. Pet. Technol. **63**, 65 (2011).
[16] T. E. Jupp and A. W. Woods, J. Fluid Mech. **484**, 329 (2003).
[17] O. Manickam and G. M. Homsy, Phys. Fluids A **5**, 1356 (1993).